

A Non-Parametric Reconstruction of the Electron Pressure Profile in CLJ1226.9

C. Romero¹ *, M. McWilliam^{2,3}, J.-F. Macías-Pérez², and NIKA collaboration

¹ Institut de RadioAstronomie Millimétrique (IRAM), Grenoble, France

² Laboratoire de Physique Subatomique et de Cosmologie, Université Grenoble Alpes, CNRS/IN2P3, 53, avenue des Martyrs, Grenoble, France

³ Imperial College London, Kensington, London SW7 2AZ, UK

Received June 22, 2017 / Accepted –

Abstract

We present the non-parametric pressure profiles of the galaxy cluster CLJ 1226.9+3352 as determined from SZ data from the MUSTANG, NIKA, Bolocam, and Planck instruments. These instruments all probe different angular scales. Given the ability of Planck to constrain the total signal, we include a prior on the integrated Compton Y parameter as determined by Planck. Our non-parametric algorithm makes use of logarithmic interpolation, which under the assumption of ellipsoidal symmetry is analytically integrable. For MUSTANG, NIKA, and Bolocam we derive a non-parametric pressure profile independently and find good agreement among our instruments. In particular, we find that the non-parametric profiles are consistent with a fitted gNFW profile. For a given instrument, constraints on the pressure profile diminish rapidly beyond the field of view. The overlap in spatial sensitivity of these three datasets is therefore critical in checking for consistency between instruments. Our analysis of CLJ 1226.9+3352 covers a large radial range: $0.05R_{500} < r < 2R_{500}$ provides a wider range of sensitivity than is typical of SZ studies thus far.

Key words. – Galaxies: clusters: individual: CLJ1226.9+3352

1. Introduction

In recent years, Sunyaev Zel’dovich (SZ) effect observations have seen an increase in high resolution ($\theta \lesssim 30''$) observations (e.g. Mason et al. 2010; Adam et al. 2014; Kitayama et al. 2016). These observations come from MUSTANG on the Robert C. Byrd Green Bank Telescope (GBT Dicker et al. 2008), NIKA on the IRAM 30-meter telescope (Monfardini et al. 2010), and ALMA, band 3 observations. However, all of these high resolution instruments have been limited in their ability to recover signal at large scales (beyond $\sim 45''$ for MUSTANG and ALMA, and $\sim 100''$ for NIKA). As galaxy clusters have characteristic radii, $R_{500} \gtrsim 3'$, SZ observations made with these instruments have not been able to recover the entire signal of the observed galaxy clusters. Therefore, observations from SZ instruments which recover SZ at larger scales such as Bolocam Czakon et al. (2015) or Planck (Planck Collaboration et al. 2013b) have been used in Romero et al. (2015) and Adam et al. (2014) respectively.

These joint analyses have shown the ability to constrain the pressure profile of the intracluster medium (ICM) of individual galaxy clusters over a large spatial range, often by assuming some parameterized pressure profile (e.g. Romero et al. 2016; Adam et al. 2014). In Romero et al. (2015), the difference in fitted pressure profiles with the addition of MUSTANG data was noted. In the case of Romero et al. (2016); Adam et al. (2014), the pairs of instruments used did not have an overlap in scales of instrument sensitivity, so the addition of another instrument would not necessarily present any discrepancies. However, as new SZ instruments like (NIKA2 Monfardini et al. 2014) and (MUSTANG2 Dicker et al. 2014) with sensitivity to a larger range of scales come online, there will be overlap, which for

clusters observed with multiple instruments, studies of the kinetic SZ effect, or relativistic corrections (Itoh et al. 1998) will be of significant interest and stand to benefit from the additional frequency coverage. To be sure of the results of these analyses, it will be critical to understand any systematics involved with individual instruments. Recent results combining Bolocam and Planck data (Sayers et al. 2016), which overlap in regions of sensitivity, show non-trivial changes from previous Bolocam-only results (Sayers et al. 2013).

While some SZ studies have reconstructed non-parametric pressure profiles either through a maximum-likelihood approach (e.g. Ruppen et al. 2017) or deprojection of their data (e.g. Basu et al. 2010; Sayers et al. 2013), such studies appear far outnumbered by the SZ analyses which have fit a parametric (smooth) pressure profile to their data. Over a decade ago, the beta model (Cavaliere & Fusco-Femiano 1978) was favored; more recently other parameterizations such as a self-similar (Mroczkowski et al. 2009) and analytical pressure profile based on a polytropic equation of state (Bulbul et al. 2010) have been explored. Yet, the generalized Navaro-Frenk-and-White (gNFW Nagai et al. 2007) profile has garnered the most traction, with a fairly canonical set of parameters coming from Arnaud et al. (2010) (Hereafter, A10).

Investigating cluster pressure profiles non parametrically will show deviations from a smooth pressure profile. Without artificially smoothing our profiles, we are thus better positioned to understanding sources of systematic error of individual instruments as well as revealing any true departures from a smooth pressure profile. Departures from a smooth pressure profile may indicate a departure from hydrostatic equilibrium (Basu et al. 2010).

* Corresponding author: Charles Romero, romero@iram.fr

Counts of galaxy clusters by mass and redshift serve to constrain cosmological parameters, notably the dark energy density (Ω_Λ), dark matter density (Ω_{dm}), the amplitude of fluctuations (σ_8), and the equation of state of dark energy (w). Constraints on these parameters derived from galaxy cluster samples are generally limited by the accuracy of mass estimation of galaxy clusters (e.g. [Hasselfield et al. 2013](#); [Reichardt et al. 2013](#)). Scaling relations which relate global (integrated) observables to the cluster mass are often employed. Currently, scaling relations as applied to observables over an intermediate radial region of galaxy clusters is preferred as this range shows minimal scatter in the scaling relations (e.g. [Kravtsov & Borgani 2012](#)) owing to the generally low cluster-to-cluster scatter in pressure profiles, found observationally and in simulations, within this radial range (e.g. [Borgani et al. 2004](#); [Nagai et al. 2007](#); [Arnaud et al. 2010](#); [Bonamente et al. 2012](#); [Planck Collaboration et al. 2013b](#); [Sayers et al. 2013](#)). While the relative homogeneity of pressure profiles in the intermediate region is well evidenced, it remains important to develop methods to derive non-parametric pressure profiles of clusters so that physical deviations are not artificially smoothed by the adoption of a given smooth parametric profile.

This paper is organized as follows. In Section 2 we review the NIKA, MUSTANG, and Bolocam observations and reduction. In Section 3 we address the method used to non-parametrically fit pressure profiles to each of the data sets. Throughout this paper we assume a Λ CDM cosmology with $\Omega_m = 0.31$, $\Omega_\Lambda = 0.69$, and $H_0 = 68 \text{ km s}^{-1} \text{ Mpc}^{-1}$, consistent with the cosmological parameters derived from the full *Planck* mission ([Planck Collaboration et al. 2016](#)).

2. Observations and Data Reduction

2.1. CLJ1226.9+3352

At a redshift of $z = 0.89$, CLJ1226.9+3352, hereafter CLJ 1227, is a massive cluster which was first discovered in the Wide Angle ROSAT Pointed Survey (WARPS [Ebeling et al. 2001](#)). It has successively been well studied in the X-ray (*XMM*, *Chandra*, and *XMM/Chandra* [Maughan et al. 2004](#); [Bonamente et al. 2006](#); [Maughan et al. 2007](#), , respectively) and SZ ([Joy et al. 2001](#); [Muchovej et al. 2007](#); [Mroczkowski et al. 2009](#); [Mroczkowski 2011](#); [Bulbul et al. 2010](#); [Korngut et al. 2011](#); [Adam et al. 2015](#)). In [Maughan et al. \(2007\)](#), the identification of hot southwestern component gave the first indications of disturbance in this cluster. This interpretation was further bolstered by HST observations ([Jee et al. 2009](#)), in which the lensing analysis revealed two distinct peaks, one of which was coincident with the hot X-ray temperature region.

Given the relative circular symmetry of CLJ 1227, it provides a suitable test for determining a non-parametric pressure profile of the cluster, while maintaining the assumption of spherical symmetry. For the centroid, we adopt the X-ray centroid from ACCEPT ([Cavagnolo et al. 2009](#)) is at [RA,Dec] = [12:26:57.9,+33:32:49] (J2000). From X-ray data, [Mantz et al. \(2010\)](#) find a scale radius $R_{500} = 1000 \text{ kpc}$, which corresponds to $M_{500} = 12.0 \times 10^{14} M_\odot$.

2.2. NIKA Observations and Reduction

We use in this paper NIKA camera observations of the cluster CLJ 1227, which were obtained at the IRAM 30 m telescope (Pico Veleta) in February 2014 and presented in [Adam et al. \(2015\)](#). NIKA ([Monfardini et al. 2010, 2014](#)) was a dual band camera working at 150 and 260 GHz, and consisted of

253 Kinetic Inductance Detectors (KIDs) operating at 100 mK by using a closed cycle ^3He - ^4He dilution fridge. Furthermore, with a sensitivity of $14 \text{ (35) mJy/beam.s}^{1/2}$, a circular field-of-view (FOV) of $1.9' \text{ (1.8')}$, and a resolution of $18.2'' \text{ (12.0'')}$ at 150 (260) GHz NIKA was particularly well adapted to map the thermal Sunyaev-Zeldovich effect in such a high redshift cluster. Including calibration and bandpass uncertainties, the NIKA conversion factors from mJy/beam to Compton parameter are -10.9 ± 0.8 and 3.5 ± 0.5 at 150 and 260 GHz, respectively. A detailed description of the general performances of the camera can be found in [Catalano et al. \(2014\)](#); [Adam et al. \(2014\)](#).

CLJ 1227 was mapped using on-the-fly raster scans with an on-cluster time of 7.8 hours. Pointing offsets were corrected during observations, achieving an overall pointing RMS error below $3''$. Uranus was used as a primary calibrator with overall calibration uncertainties of 7% and 12% at 150 and 260 GHz, respectively. The NIKA raw data was processed using the NIKA processing pipeline described in [Adam et al. \(2014\)](#) and [Adam et al. \(2015\)](#). Low frequency atmospheric emission was removed using a common mode, which was computed iteratively after masking in the time domain the reconstructed cluster signal to a given signal-to-noise threshold. The processed data were gridded into $2''$ square pixels using inverse variance weighting and nearest grid projection. The transfer function of the processing procedure was computed using signal plus noise simulations as described in [Adam et al. \(2015\)](#). A full representation of the obtained transfer function is given in Figure 3 of [Adam et al. \(2015\)](#) and it is used in this paper. Overall the transfer function is consistent with a constant value of 1 for angular scales smaller than the NIKA FOV and larger than the size of the NIKA beam. Using the 260 GHz NIKA map [Adam et al. \(2015\)](#) identified a point source located $30''$ southeast of the center of the cluster. The 150 GHz NIKA map, with the point source subtracted (Section 3.1) is shown in the middle panel in Figure 1.

2.3. MUSTANG Observations and Reduction

The MUSTANG camera ([Dicker et al. 2008](#)) on the 100 meter Robert C. Byrd Green Bank Telescope (GBT, [Jewell & Prestage 2004](#)) with its angular resolution of $9''$ (full-width, half-maximum FWHM) is one of only a few SZ effect instruments with sub-arcminute resolution. However, MUSTANG's instantaneous field of view (FOV) limits its sensitivity to scales larger than $1'$. MUSTANG is a 64 pixel array of Transition Edge Sensor (TES) bolometers arranged in an 8×8 array located at the Gregorian focus on the 100 m GBT. Operating at 90 GHz (81–99 GHz), MUSTANG has an angular resolution of $9''$ and pixel spacing of $0.63 f/\lambda$ resulting in a FOV of $42''$. The conversion factor from Jy/beam to Compton parameter used is 2.50. More detailed information about the instrument can be found in [Dicker et al. \(2008\)](#).

Our observations and data reduction are described in detail in [Romero et al. \(2015\)](#), and we briefly review them here. Absolute flux calibrations are based on the planets Mars, Uranus, or Saturn, nebulae, or the star Betelgeuse (α_{Ori}). Responsive detectors are determined by scans taken at regular intervals with a calibration lamp. We fit and subtract a common mode template, polynomial, and sinusoid. Further data quality checks are calculated after this subtraction. The MUSTANG data map, with the point source subtracted (see Section 3.1) is shown in the left panel in Figure 1.

We refine the the transfer function found in [Romero et al. \(2016\)](#) by filtering a cluster model using a strictly A10 profile (a gNFW profile with parameters

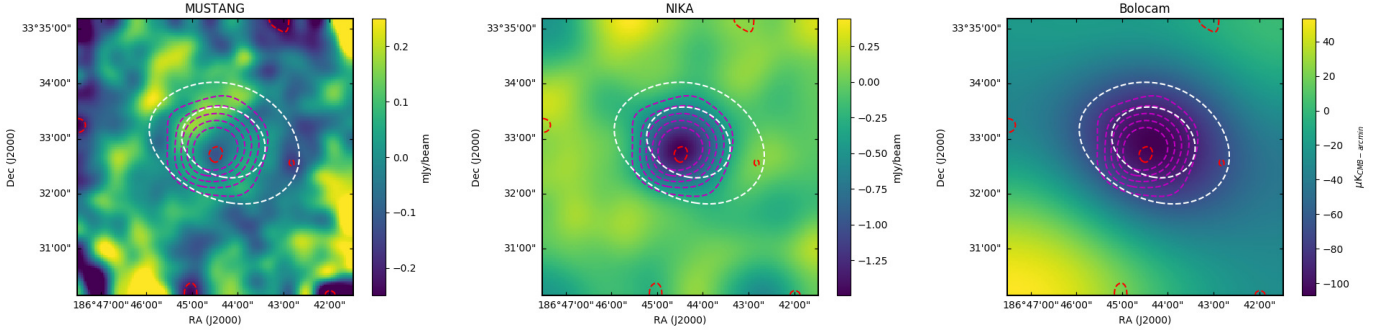


Figure 1. Left: MUSTANG map; Middle: NIKA (2mm) map; Right: Bolocam map. In all three panels, the red contours are those of MUSTANG, magenta contours of those of NIKA, and white contours are those of Bolocam. For MUSTANG and Bolocam, the contours start at $(-2)\sigma$, with 1σ increments. For NIKA, the contours start at $(-3)\sigma$ with 2σ increments. The point source identified in Adam et al. (2015) is subtracted in the MUSTANG and NIKA maps.

Table 1. Overview of the sensitivities achieved for each of the instruments used in this analysis.

Instrument	Freq. (GHz)	T_{obs} (hours)	Noise (Compton y)	FWHM ($''$)	FOV ($''$)
NIKA	150	7.2	12.5×10^{-6}	18	1.9
MUSTANG	90	4.9	34.2×10^{-6}	9	0.7
Bolocam	140	11.8	8.48×10^{-6}	58	8

$[\alpha, \beta, \gamma, C_{500}, P_0] = [1.05, 5.49, 0.31, 1.18, 8.42P_{500}]$ through the standard MUSTANG pipeline. The resultant transfer function is then merged with the previous transfer function (calculated on white noise). The principle difference between this new transfer function and the former transfer function occurs at scales larger than the FOV (wavenumbers smaller than ~ 0.025 inverse arcseconds). We check the robustness of the transfer functions to the standard pipeline across a range of cluster models (gNFW profiles with varying parameters) and find agreement, principally of the peak amplitude, within 10%.

Moreover, we verify the fidelity of the new transfer function by reproducing the analysis performed in Romero et al. (2016) for CLJ1227, with the use of the new transfer function in place of the standard MUSTANG filtering procedure. In general, we find good agreement for the constraints on pressure profiles. More specifically, cluster models with $0.5 < C_{500} < 3.3$ are well reproduced with fitted amplitudes that are within 10% of those found in Romero et al. (2016). Furthermore, the best fit profile shape parameters (C_{500} , P_0 , and γ) are within $\sim 10\%$ agreement as well.

2.4. Bolocam Observations and Reduction

To probe a wider range of scales we complement our MUSTANG data with SZ data from Bolocam (Glenn et al. 1998). Bolocam is a 144-element bolometer array on the Caltech Submillimeter Observatory (CSO) with a beam FWHM of $58''$ at 140 GHz and circular FOV with $8'$ diameter, which is well matched to the angular size of R_{500} ($\sim 2'$) of the clusters in our sample. Bolocam's conversion factor to Compton y from μK_{CMB} is reported as -3.69×10^{-7} , with the relativistic corrections taken into account.

Bolocam is a 144-element camera that was a facility instrument on the Caltech Submillimeter Observatory (CSO) from 2003 until 2012. Its field of view is $8'$ in diameter, and at 140 GHz it has a resolution of $58''$ FWHM (Glenn et al. (1998);

Haig et al. (2004)). The clusters were observed with a Lissajous pattern that results in a tapered coverage dropping to 50% of the peak value at a radius of roughly $5'$, and to 0 at a radius of $10'$. The Bolocam maps used in this analysis are $14' \times 14'$. The Bolocam data are the same as those used in Czakon et al. (2015) and Sayers et al. (2013); the details of the reduction are given therein, along with Sayers et al. (2011). The (2mm) Bolocam map is shown in the right panel of Figure 1. The reduction and calibration is similar to that used for MUSTANG, and Bolocam achieves a 5% calibration accuracy and $5''$ pointing accuracy.

2.5. Planck integrated Compton parameter

As in Adam et al. (2015) we consider in the analysis the integrated Compton parameter of the cluster as measured using the Planck data. We use the Planck frequency maps from 143 to 857 GHz to produce a Compton parameter map as described in Hurier et al. (2013) and Planck Collaboration et al. (2013a); ?. The resolution of this map is $7.5'$, limited by the lowest frequency Planck channel map used in the reconstruction. Using this map we compute the integrated Compton parameter up to a radial distance of $15'$ with respect to the center of the cluster. Uncertainties in the integrated Compton parameter are computed by integrating at random positions around the cluster. The uncertainties obtained have been also cross checked using Planck half-ring half difference Compton parameter map obtained as described in Planck Collaboration et al. (2013a); ?. We find $Y_{15'} = (0.94 \pm 0.36) \times 10^{-3}$ arcmin 2 .

3. Non-parametric Pressure Profile Reconstruction via a Maximum Likelihood Analysis

3.1. Preprocessing

A point source at 4.6σ significance (~ 0.5 mJy) in MUSTANG was reported in Korngut et al. (2011), but is not evident in the

reprocessed MUSTANG data. A short VLA filler observation (VLA-12A-340, D-array, at 7 GHz) was performed to follow up this potential source (at RA 12:26:58.0 and Dec +33:32:59), but to a limit of $\sim 50\mu\text{Jy}$ nothing is seen. At $500\mu\text{m}$, *Herschel-SPIRE* has a point source sensitivity of $\sim 8\text{ mJy}$, and therefore does not truly constrain a potential point source at this location.

In addition, Adam et al. (2015) find a point source at RA 12:27:00.01 and Dec +33:32:42 with a flux density of 6.8 ± 0.7 (stat.) ± 1.0 (cal.) mJy at 260 GHz and 1.9 ± 0.2 (stat.) at 150 GHz. At $500\mu\text{m}$, *Herschel-SPIRE* finds a flux of $100 \pm 8\text{ mJy}$.¹ A point source at this location is fit to the MUSTANG data with a flux density of $0.36 \pm 0.11\text{ mJy}$ (Romero et al. 2016). We subtract this point source from the NIKA and MUSTANG maps using the above flux density values.

The mean level in the MUSTANG map is calculated as the mean within the inner arcminute MUSTANG noise map. We subtract the mean level from the MUSTANG map before fitting a cluster model. The Bolocam map already has a mean level subtracted. The point source is faint enough to not be a concern for the Bolocam data given Bolocam’s beam size. No mean level is subtracted from NIKA.

3.2. Non-Parametric Pressure Profile Models

We employ a spherically symmetric pressure profile as our galaxy cluster model. Our fitting algorithm is applied to each dataset independently; therefore, cluster models are binned and gridded differently for each dataset. Radial bins are defined so that each bin is at least as wide as a beam width, with the additional constraint that the outer most bin is beyond the FOV of the instrument. We define our radial bins based on the radii which confine the bins. Our first bin covers the range $0 < r < R_1$; our second bin covers $R_1 < r < R_2$, and our last (n th) bin covers $R_{n-1} < r$, i.e. it extends to infinity. A finite radius R_n is defined, and is used to determine the power law in this outermost bin. Pressure normalizations, P_i , are defined at each bin boundary, R_i . We then assume that the pressure in between bin boundaries follows a power law, $P \propto r^{-\alpha}$. We assume that the power law in the first bin is given by the power law of the second bin. The power law of the outermost bin is determined from P_{n-1} (at R_{n-1}) and P_n (at R_n), and extended to infinity. Given the integration along the line of sight, we put a prior on this outer bin such that $\alpha > 1$. We note that under hydrostatic equilibrium (HSE), this should be limited to $\alpha > 3$ in order to avoid having infinite mass.

Given the restrictions of elliptical symmetry and a power law dependence of the integrated quantity (pressure) on the elliptical radius, it is possible to calculate the integral along the line of sight analytically (e.g. Vikhlinin et al. 2001; Korngut et al. 2011). We follow principally the formulation provided in Korngut et al. (2011). As noted in Sarazin et al. (2016), there are certain power laws ($\alpha/2 = p = 1/2, 0, -1/2, -1, -3/2, \dots$) for which the formulation given in Korngut et al. (2011) fails, but a reformulation provides a valid integration. More generally, the formulation fails for $\alpha/2 = p < -1/2$. While a negative index indicates a rise in pressure with radius (atypical), this could arise, especially localised, from shocks, for example. We also wish to minimise our restrictions on the power laws (between bins) so as to minimise induced correlations between bins. Therefore, we implement extensions to the canonical formulation that allow us to integrate within finite regions (spheres or shells that extend only to a finite radius). These extensions and reformulations of specific half integers are described in Appendix A.

¹ <http://irsa.ipac.caltech.edu/applications/Gator/>

The integrated profiles, calculated as the Compton y parameter:

$$y = \frac{\sigma_T}{m_e c^2} \int P_e dl, \quad (1)$$

are converted into the units of the original data map. Maps are gridded by assuming a linear interpolation of the 1D (radial) profiles. When gridding our bulk ICM component, we adopt the ACCEPT centroid of CLJ 1227. These maps are then convolved with the respective beam and transfer function.

3.3. Fitting Algorithm

We employ a maximum likelihood algorithm, and take our noise to be Gaussian such that our likelihood is given by:

$$\mathcal{L} \propto e^{-\chi^2/2} \quad (2)$$

and χ^2 is given by:

$$\chi^2 = (\vec{d} - \vec{d}_{mod})^T \mathbf{N}^{-1} (\vec{d} - \vec{d}_{mod}), \quad (3)$$

where \vec{d} is our data, \vec{d}_{mod} is our model, and \mathbf{N}^{-1} is our covariance matrix for a given dataset.

In previous works, NIKA and MUSTANG noise has been taken as uncorrelated (e.g. Romero et al. 2015, 2016; Adam et al. 2015). Bolocam noise has been taken as roughly uncorrelated, but 1000 noise realizations, which included CMB and point source estimates, are provided to allow for a more accurate noise estimation (Sayers et al. 2011). We calculate the two-dimensional power spectrum for noise maps of each dataset and find that the noise is consistent with white noise on the scales, for each dataset, which we wish to constrain the models.

We calculate the final probability of our models by applying priors as prescribed by Bayes’ Theorem. On each of the pressure bins, we assign strict priors that $P_i > 0$, and as previously mentioned, the last bin has a prior that on its associated power law slope: $\alpha > 1$. We allow for the choice of including a prior on the integrated Compton Y parameter:

$$Y = \int y d\Omega, \quad (4)$$

where the integral over solid angle taken within a given radius is generally referred to as the cylindrical Compton Y value (Y_{cyl}). We calculate Y_{cyl} using the un-filtered Compton y profile (before convolution with an instrument’s beam and transfer function). The prior on Y comes from Planck data (Planck Collaboration et al. 2014) as discussed in Section 2.5. In particular, we take the prior given in Adam et al. (2015): $Y_{cyl}(15') = (0.94 \pm 0.36) \times 10^{-3} \text{ arcmin}^2$.

We employ the described probability function in a python Markov Chain Monte Carlo (MCMC) package, emcee (Foreman-Mackey et al. 2013). This MCMC package makes use of a variant of a Metropolis-Hastings (MH) algorithm, in particular the ensemble sampling algorithm is affine-invariant (Goodman & Weare 2010). The use of ensemble sampling, as opposed to a canonical single-point sampling, contributes to the notable advantage of this algorithm (within emcee) having a much shorter autocorrelation time than a standard MH algorithm. Furthermore, the computationally expensive part of drawing a new walker has been parallelized.

3.4. Robustness of Fitting Algorithm

Our algorithm is first tested with mock cluster observations. We create mock observations by adding a noise realization (created from jack-knifed timestreams) for each of the three maps to the corresponding filtered map of a previously determined (Romero et al. 2016) gNFW profile. The fits to our mock observations recover the input gNFW profile well, as shown in Figure 2; however, especially for the Bolocam fits, the two outermost bins are biased high.

We also compare our non-parametric fits with power-law interpolation between bins (our default), to non-parametric fits with uniform pressure within a bin. We find that the non-parametric fits with uniform pressure are much more sensitive to the number of bins, as indeed, the transfer functions of the various instruments, especially MUSTANG, substantially reduce the signal from extended (uniform) structure.

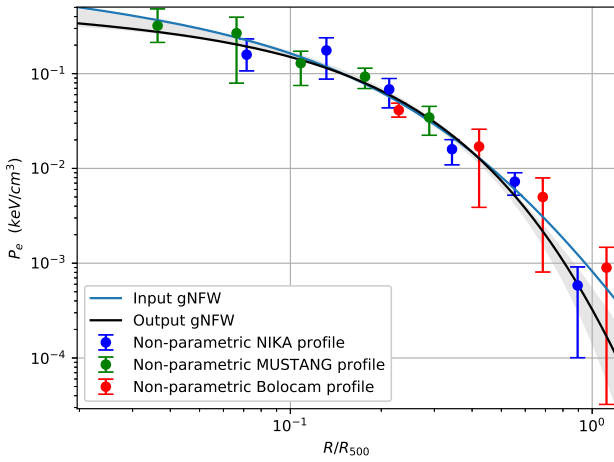


Figure 2. Non-parametric pressure profiles as determined via each simulated observation individually, and the gNFW (parametric) pressure profile as simultaneously fit to the non-parametric pressure profiles. The error bars are statistical, from the MCMC fits.

Our non-parametric fits recover consistent pressure profiles given different starting positions and bin spacing. Additionally, we find that our pressure profiles are consistent with those produced when using uniform pressure bins (as opposed to using interpolated power laws). This is true of persistent features, especially those seen at large radii in Bolocam data, where the transfer function shows a notable ringing effect. A drawback of our modelling algorithm is that our requirement that the outer slope be greater than 1 results in our outer two bins, in the Bolocam fits, being affected by the ringing effect, over a wider range of bin spacing.

The outermost bins appear to be affected by systematics from the transfer function, of the respective instrument. Therefore, except for NIKA, where we impose priors to constrain the integrated signal, we do not consider the last bin in further analysis. However, we find that these outermost bins appear important to include within the fitting procedure. In the case of Bolocam, we find the transfer function appears to also impose a systematic offset on the second-to-last bin as well. Therefore, it too is trimmed.

We find that the use of 6 bins provides generally reliable results. Use of more bins results in larger error bars, while the use of few bins reduces resolution, thereby smoothing out interesting features revealed in our pressure profiles.

4. Non-Parametric Pressure Profile Results

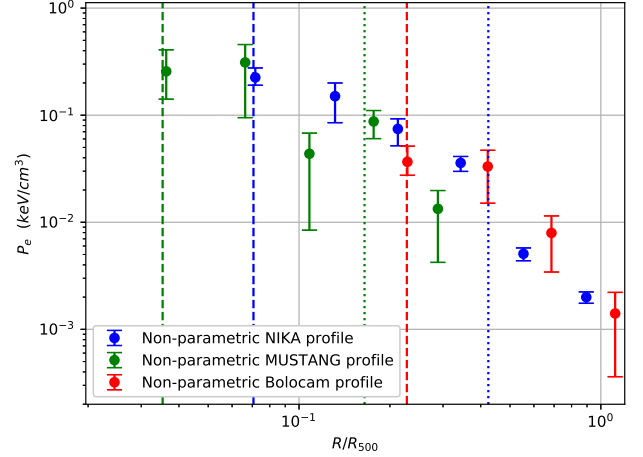


Figure 3. Non-parametric pressure profiles as determined via each dataset individually, and the gNFW (parametric) pressure profile as simultaneously fit to the non-parametric pressure profiles. The error bars are statistical, from the MCMC fits. The vertical dashed and dotted lines correspond to the half width half maximum (HWHM) and FOV/2 (i.e. radial FOV), respectively; the coloring is also respective to each instrument.

Given the MUSTANG transfer function, we expect that the constraints beyond the 42'' (radially) are negligible. Therefore, we exclude the outermost radial bin from further analysis. The Bolocam transfer function is provided as a two-dimensional transfer function. We find that the transfer function produces artifacts at large radii ($r \gtrsim 1000$ kpc) for all plausible cluster models. While we find it important to include these outer bins for the fitting procedure itself, we exclude the outer two bins from further analysis. The results, after these exclusions, are tabulated in Table 2.

From the monte carlo chains of the non-parametric fits, we determine the covariance matrix of the pressure bins for each dataset as:

$$\mathbf{N}_{i,j} = \langle d_i d_j \rangle - \langle d_i \rangle \langle d_j \rangle. \quad (5)$$

We show the correlation matrices in Figure 4. We notice that any two adjacent bins are negatively correlated, and by extension, bins spaced 2 apart (e.g bins 1 and 3) are positively correlated. The maximum amplitude of these correlations is 0.05, 0.13, and 0.05 for NIKA, MUSTANG, and Bolocam respectively.

5. Parametric Fits: gNFW

We wish to compare our non-parametric fits to each other and to previous results. Given the ubiquity of parametric pressure profiles, and in particular, the gNFW parameterization, we fit a

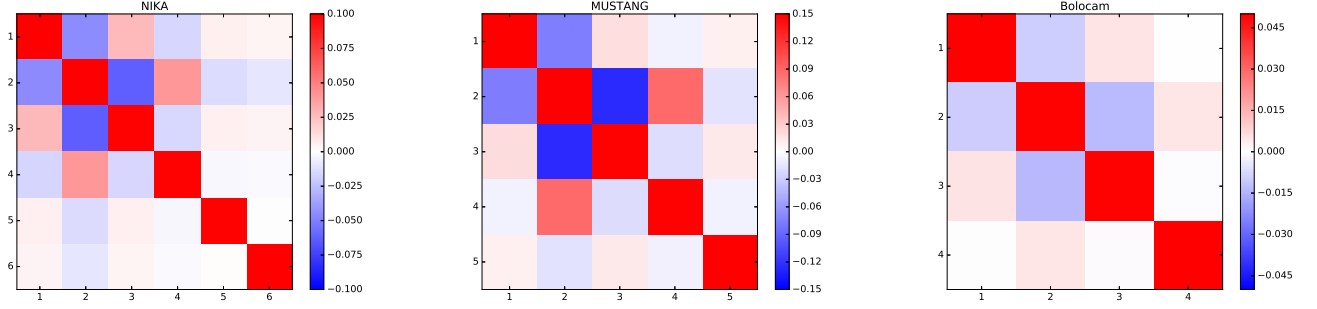


Figure 4. Left: NIKA correlation Matrix. Middle: MUSTANG correlation matrix. Right: Bolocam correlation matrix. The coloring is scaled to make the magnitude of off-diagonal terms more apparent, and the range changes for each instrument.

Table 2. Non parametric pressure profile fits.

R (kpc)	P_e (keV cm ⁻³)	$\sigma_{P_e,low}$ (keV cm ⁻³)	$\sigma_{P_e,high}$ (keV cm ⁻³)
NIKA			
73	0.225	0.051	0.035
134	0.150	0.049	0.065
216	0.0744	0.0181	0.0226
349	0.0358	0.0053	0.0060
564	0.00508	0.00068	0.00071
910	0.00200	0.00024	0.00024
MUSTANG			
37	0.257	0.151	0.115
67	0.311	0.146	0.216
110	0.0436	0.0243	0.0352
180	0.0874	0.0231	0.0270
294	0.0133	0.0064	0.0091
479	0.000959	0.00082	0.00284
Bolocam			
233	0.0367	0.0147	0.0092
429	0.0332	0.0139	0.0181
698	0.00795	0.0035	0.0045
1135	0.00141	0.00081	0.00104
1845	0.00320	0.00083	0.00084
3000	0.00101	0.00044	0.00047

gNFW profile to our non-parametric pressure profile constraints. The gNFW profile is given as:

$$\tilde{P} = \frac{P_0}{(C_{500}X)^\gamma [1 + (C_{500}X)^\alpha]^{(\beta-\gamma)/\alpha}} \quad (6)$$

where $X = R/R_{500}$, and C_{500} is the concentration parameter; one can also write $(C_{500}X)$ as (R/R_p) , where $R_p = R_{500}/C_{500}$. The exponentials α , β , and γ are commonly cited as the (logarithmic) slopes at moderate, large, and small radii. However, α can be less than γ , or greater than β , without the profile attaining such a slope. Therefore, α should be understood as influencing the rate of turnover between the two slopes, β and γ .

We aim to constrain all parameters within the gNFW profile, but find that α is driven to high values, and furthermore the constraints are very poor for this high values. Therefore, we choose to restrict α to 1.05, the value found in [Arnaud et al. \(2010\)](#). We further include nuisance parameters of calibration offsets for each dataset. The calibration uncertainties for NIKA, MUSTANG, and Bolocam are taken to be 7%, 10%, and 5% respectively. The mean level in each dataset has already been

removed or fitted, so it is not considered here. We use the full covariance matrices from our non-parametric fits.

5.1. Parametric Constraints

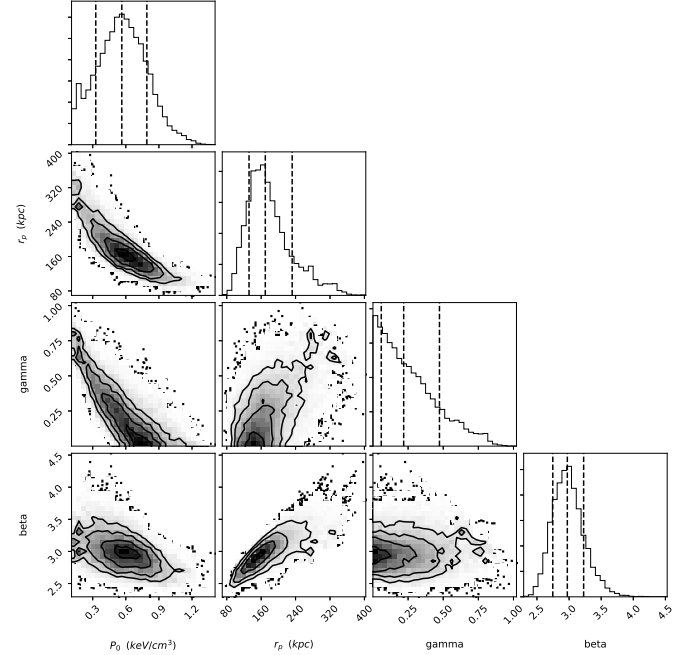


Figure 5. Parameter constraints for our gNFW model: P_0 , r_p , γ , and β . Recall that $C_{500} = r_p/R_{500}$.

We find gNFW parameters of $[P_0, C_{500}, \beta, \text{ and } \gamma] = [49.7^{+22.4}_{-24.9}, 5.89^{+1.94}_{-1.78}, 2.98^{+0.28}_{-0.23}, \text{ and } 0.23^{+0.30}_{-0.17}]$. The power law slope γ is within expected value range given previous gNFW constraints, on CLJ1226 as well as general cluster samples. However, our value of β is less than expected; moreover, under hydrostatic equilibrium $\beta \leq 3$ would indicate an unbounded mass at arbitrarily large radii. Similarly, P_0 and C_{500} are larger than generally found. Given the degeneracy between β , P_0 , and C_{500} , as shown in Figure 5, and shape of the pressure profile, these atypical values of β and P_0 appear to be driven by C_{500} being pushed to larger values, where a large C_{500} value indicates

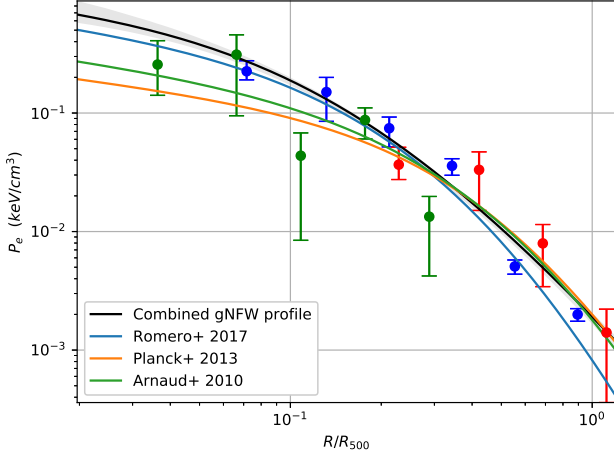


Figure 6. The gNFW (parametric) pressure profile as simultaneously fit to the non-parametric pressure profiles. The error bars are statistical, from the MCMC fits. The vertical dashed and dotted lines correspond to the HWHM and FOV/2 (i.e. radial FOV), respectively; the coloring is also respective to each instrument. The MUSTANG and NIKA points that fall below the gNFW pressure profile (close to $0.1 R_{500}$) are of note and discussed in Section 6.

that the scale radius (transition in pressure profile slopes) occurs are a relatively small radius.

We also note that the value of C_{500} itself may not be nearly as high if a smaller value of R_{500} is adopted (implying a smaller M_{500} and P_{500} .) This may well be the case, as several other studies conclude that $R_{500} < 1000$ kpc (e.g. Rumsey et al. 2016; Mroczkowski et al. 2009). Figure 6 shows our gNFW fit and comparative gNFW profiles from the literature.

6. Discussion

Our non-parametric fits show good reproducibility given different input parameters (Section 3.4). This procedure is can be readily applied to elliptical cluster geometries, and could also be modified to include shock components (Appendix). Given the potential for elliptical clusters and presence of shocks, we find that the ability to analyze both the global and local electron pressure in clusters within a non-parametric approach will be of considerable utility as sensitive, high-resolution, SZ observations of individual clusters become more commonplace.

While our estimation of outer pressure bins may be influenced by the mean level in a map, or a poorly constrained transfer function, we see that the inner bins remain largely unaffected (Section 3.4). We find generally good agreement in our non-parametric fits between MUSTANG, NIKA, and Bolocam. The fitted gNFW profile reinforces this claim, as all but two points lie within 2.5σ of the fitted curve. The inner point that falls below the gNFW profile comes from MUSTANG fits, and is only $\sim 2\sigma$ discrepant from the gNFW profile.

This deviation (at $\sim 12''$, radially) is consistent with the location of the point source found in Korngut et al. (2011), and performing the a fit on virtual data, we find that a 0.5 mJy source (at 90 GHz) can reproduce the observed deviation. Within the NIKA (150 GHz) data, no evidence for a weak point source is seen, although, we note that simulated observations of a 1.4 mJy source

at the same radial distance does not have a significant effect on the non-parametric fits, relative to the fits of the simulated observations without a point source. At other wavelengths, in the 260 GHz NIKA data (Adam et al. 2015), as well as at lower frequencies and higher frequencies (Section 3.1), no evidence is seen for a point source.

Within our gNFW fits, if α is left unconstrained, we find that large values of α are preferred, indicating a rapid transition between the inner and outer pressure profile slopes. This turnover is largely driven by NIKA, which best covers the spatial region where this transition occurs, and additionally, NIKA has the strongest detection of the cluster and places the greatest constraints on the pressure profile, globally.

6.1. Comparison with Previous SZ Results

From the first SZ measurements of CLJ 1227 (made with BIMA Joy et al. 2001) has generally appeared azimuthally symmetric and relaxed. Later studies with SZA (Muchovej et al. 2007; Mroczkowski et al. 2009; Mroczkowski 2011) all appear to reaffirm this symmetry, while the evidence in SZ observations for a potential disturbance in the core region begins to grow. Korngut et al. (2011) find a ridge of significant substructure in MUSTANG data, which when compared with X-ray profiles, is consistent with a merger scenario within CLJ 1227. However in the current processing of MUSTANG data (Romero et al. 2016), this substructure is not evident. Combining the SZ pressure profile with X-ray electron density profile, Adam et al. (2015) find relatively large entropy values in the core as support for disturbance on small scales. A similar conclusion is reached by Rumsey et al. (2016), who find that the core of CLJ 1227 exhibits signs of merger activity, while the outskirts appear relaxed.

We find that the deviations from a more canonical gNFW pressure profile (e.g. A10 profile) in our non-parametric fits and parametric fits are consistent with the narrative that the inner region of CLJ 1227 is disturbed. In particular, our non-parametric fits give an indication that the departure from a gNFW profile is marked by a pressure drop at a cluster-centric radius of $\sim 14''$ (~ 100 kpc), where MUSTANG data is critical to determining the location of this pressure deviation.

7. Conclusions

We developed an algorithm to determine a non-parametric pressure profile for galaxy clusters. This method is of particular utility to SZ observations, where the filtering effects from data processing favor model fitting, as opposed to deriving non-parametric pressure profiles via geometric deprojection. Our fitting algorithm is robust with respect to input parameters, bin spacing, and instrumental setup specifics. While the constraints of single-dish SZ observations beyond the FOV for a given instrument are generally poor, we find that the inclusion of such a bin appears to improve the robustness of the pressure constraints within the FOV.

We have applied this algorithm to SZ observations of CLJ 1227 from MUSTANG, NIKA, and Bolocam. In doing so, we cover a radial range $0.05R_{500} < r < 2R_{500}$ with continuous sensitivity and find consistency among the non-parametric fits of the individual instruments. Furthermore, parametric best fits indicate a gNFW profile with a relatively small scale radius (r_p) ($r_p = R_{500}/C_{500}$). If left unconstrained, α tends towards large values, indicating a rapid transition at this scale radius between the inner and outer slope. This rapid transition is consistent

across all three instruments, where NIKA is most sensitive to this transition region and indeed NIKA data alone favors a rapid transition. This rapid transition is nominally quicker with the addition of MUSTANG data due to the drop in recovered pressure at a radius, $9'' < r < 23''$.

Imperical investigations into potential point source contamination within this region ($9'' < r < 23''$) indicate that such a point source would have to be ~ 0.5 mJy at 90 GHz. A point source is not detected in lower frequency data (VLA: $\sim 50\mu\text{Jy}$ at 7 GHz and SZA: 0.2 mJy sensitivity at 30 GHz). Nor is a point source (in this region) detected in higher frequency data (NIKA 1mm and Herschel). Therefore, we find a point source to be an unlikely explanation for the dip in MUSTANG pressure between $9'' < r < 23''$.

Our non-parametric fits of the pressure profile of CLJ 1227 are consistent with a smooth (parameterized) pressure profile. Yet, we have the advantage that deviations from a parameterized pressure profile will be more evident, localized, and allow for easier investigation of potential contamination or deviations from hydrostatic equilibrium. In its current implementation, this approach is relatively intuitive, robust, and fast (due to the analytic integration). While a spherical cluster was assumed for this analysis, the approach already allows for an ellipsoidal geometry. We also foresee the potential to extend this approach to include analysis of slices within an ellipse, which will prove useful for investigating shocks.

Acknowledgements

The National Radio Astronomy Observatory is a facility of the National Science Foundation which is operated under cooperative agreement with Associated Universities, Inc. MUSTANG data was retrieved from . Original MUSTANG data was taken under NRAO proposal IDs GBT/09A-052, GBT/09C-059. Bolocam data was retrieved from The Bolocam observations presented here were obtained from the Caltech Submillimeter Observatory, which, when the data used in this analysis were taken, was operated by the California Institute of Technology under cooperative agreement with the National Science Foundation. Bolocam was constructed and commissioned using funds from NSF/AST-9618798, NSF/AST-0098737, NSF/AST-9980846, NSF/AST-0229008, and NSF/AST-0206158. Bolocam observations were partially supported by the Gordon and Betty Moore Foundation, the Jet Propulsion Laboratory Research and Technology Development Program, as well as the National Science Council of Taiwan grant NSC100-2112-M-001-008-MY3.

We would like to thank the IRAM staff for their support during the NIKA campaigns. The NIKA dilution cryostat has been designed and built at the Institut Néel. In particular, we acknowledge the crucial contribution of the Cryogenics Group, and in particular Gregory Garde, Henri Rodenas, Jean Paul Leggeri, Philippe Camus. This work has been partially funded by the Foundation Nanoscience Grenoble, the LabEx FOCUS ANR-11-LABX-0013 and the ANR under the contracts “MKIDS”, “NIKA” and ANR-15-CE31-0017. This work has benefited from the support of the European Research Council Advanced Grant ORISTARS under the European Union’s Seventh Framework Programme (Grant Agreement no. 291294). We acknowledge fundings from the ENIGMASS French LabEx (R. A. and F. R.), the CNES post-doctoral fellowship program (R. A.), the CNES doctoral fellowship program (A. R.) and the FOCUS French LabEx doctoral fellowship program (A. R.).

Appendix A: Analytic Integrals of Elliptically Symmetric Power Laws

In our non-parametric pressure bin analysis, we assume that the pressure distribution is elliptically symmetric with the following behavior:

$$\epsilon(x, y, z) = \epsilon_i \left(\frac{x^2}{a^2} + \frac{y^2}{b^2} + \frac{z^2}{c^2} \right)^{-P}, \quad (\text{A.1})$$

where ϵ_i is a normalization for the pressure within bin i ; a , b , and c are the ellipsoidal scalings of their respective axes, with the z -axis being along the line of sight, and $-2P$ is the slope of the pressure profile. We define an elliptical radius, $r_e = (\frac{x^2}{a^2} + \frac{y^2}{b^2} + \frac{z^2}{c^2})^{1/2}$. A pressure bin can be in one of three cases: (C1) a sphere of finite extent, (C2) a shell of finite extent, and (C3) a shell of infinite extent. We use these markers (C1, C2, and C3) as superscripts when writing definitions per case. The pressure distribution can be rewritten as follows:

$$\epsilon^{C1}(r_e) = \begin{cases} \epsilon_i(r_e^2)^{-P} & : r_e^2 \leq 1 \\ 0 & : r_e^2 > 1, \end{cases} \quad (\text{A.2})$$

$$\epsilon^{C2}(r_e) = \begin{cases} 0 & : r_e^2 < 1 \\ \epsilon_i(r_e^2)^{-P} & : 1 \leq r_e^2 \leq R_i^2 \\ 0 & : r_e^2 > R_i^2, \text{ and} \end{cases} \quad (\text{A.3})$$

$$\epsilon^{C3}(r_e) = \begin{cases} 0 & : r_e^2 < R^2 \\ \epsilon_i(r_e^2)^{-P} & : R_i^2 \leq r_e^2, \end{cases} \quad (\text{A.4})$$

where $R_i > 1$ is a boundary radius (the outer boundary in Case 2). Given a cluster profile with more than 3 bins, we end up with many bins in Case 2, in which case we rescale a , b , c , and subsequently R_i each time to properly normalize each bin.

Let us define

$$\kappa = \sqrt{\pi} \epsilon_i c \frac{\Gamma(P - 0.5)}{\Gamma(P)} A^{1-2P}, \quad (\text{A.5})$$

where $A^2 = (x^2/a^2) + (y^2/b^2)$. While the integration of each bin will share this expression, the actual values may change depending on a , b , and c used for each bin (as above, when multiple bins fall into Case 2). We write the integration of $\epsilon(r_e)$ along the line of sight as:

$$I = \int_{-z_0}^{z_0} \epsilon(r_e^2) dz. \quad (\text{A.6})$$

Over the three cases, the solutions are as follows:

$$I^{C1} = \begin{cases} \kappa(1 - I_{A^2}(P - 0.5, 0.5)) & : A^2 \leq 1 \\ 0 & : A^2 > 1 \end{cases} \quad (\text{A.7})$$

$$I^{C2} = \begin{cases} \kappa(I_{A^2}(P - 0.5, 0.5) - I_{A^2/R^2}(P - 0.5, 0.5)) & : A^2 < 1 \\ \kappa(1 - I_{A^2/R^2}(P - 0.5, 0.5)) & : 1 \leq A^2 \leq R^2 \\ 0 & : R^2 \leq A^2 \end{cases} \quad (\text{A.8})$$

$$I^{C3} = \begin{cases} \kappa(I_{A^2/R^2}(P - 0.5, 0.5)) & : A^2 \leq R^2 \\ \kappa & : A^2 > R^2 \end{cases} \quad (\text{A.9})$$

Here, I_{A^2} , or I_{A^2/R^2} is the incomplete beta function, often denoted as $I_x(a, b)$. For the discussion of the gamma and incomplete beta function (below), x , y , a , and b serve as dummy variables. Given our use of the gamma and incomplete beta functions, it is important to recognize their limitations. Specifically, $\Gamma(a)$ is undefined for $a = -j$, $j \in \mathbb{N} \cup \{0\}$ (negative integers, including zero). Our incomplete beta function, having $a = P - 0.5$

and $b = 0.5$ suffers from undefined values for $P = 0.5 - j$, $j \in \mathbb{N} \cup \{0\}$ as well as $P = -j$, $j \in \mathbb{N} \cup \{0\}$. Finally, all incomplete beta functions are generally defined for $B(a, b)$ that $Re(a) > 0$ and $Re(b) > 0$. However, the relation of the incomplete beta function (I_x):

$$I_x(a, b) = I_x(a + 1, b) + \frac{x^a(1 - x)^b}{aB(a, b)} \quad (\text{A.10})$$

allows us to extend our function into the negative domain (for a , which we take as $P - 0.5$).

To deal with the limitation, generally seen as: $2 * y - 2 = -j$, $j \in \mathbb{N} \cup \{0\}$, we derive another approach. From Equation A.6, we can substitute variables ($t = z/(cA)$) to arrive at:

$$I = 2\epsilon_i A^{-2P} \int_0^{t_0} (1 + t^2)^{-P} cA dt \text{ and now adopt } t^2 = \frac{u}{1 - u} \quad (\text{A.11})$$

$$= 2\epsilon_i A^{-2P} \int_0^{\theta_0} (1 + \tan^2(\theta))^{-P} \sec^2(\theta) d\theta \quad (\text{A.12})$$

$$= 2\epsilon_i A^{-2P} \int_0^{\theta_0} \cos^{2P-2}(\theta) d\theta \quad (\text{A.13})$$

This must then be extended, and is done so with the relation:

$$\int \cos^{n-2}(\theta) d\theta = \frac{n}{n-1} \int \cos^n(\theta) d\theta - \frac{1}{n-1} \cos^{n-1}(\theta) \sin(\theta) \quad (\text{A.14})$$

Given our values of interest/applicability ($2y - 2 = -j$, $j \in \mathbb{N} \cup \{0\}$), this extension is perfectly applicable, and we will end in nice functions; either:

$$\begin{aligned} \int \cos^n(\theta) d\theta &= \tan(\theta) \text{ for } n = -2 \text{ or:} \\ \int \cos^n(\theta) d\theta &= \ln |\sec(\theta) + \tan(\theta)| \text{ for } n = -1 \end{aligned}$$

The **only** place where this analytic integration fails is for $P < 0.5$ **when** integrating out to infinity, which is fine, as this must diverge in any case.

References

- Adam, R. et al. 2015, A&A, 576, A12, 1410.2808
 —. 2014, A&A, 569, A66, 1310.6237
 Arnaud, M., Pratt, G. W., Piffaretti, R., Böhringer, H., Croston, J. H., & Pointecouteau, E. 2010, A&A, 517, A92, 0910.1234
 Basu, K. et al. 2010, A&A, 519, A29, 0911.3905
 Bonamente, M. et al. 2012, New Journal of Physics, 14, 025010, 1112.1599
 Bonamente, M., Joy, M. K., LaRoque, S. J., Carlstrom, J. E., Reese, E. D., & Dawson, K. S. 2006, ApJ, 647, 25, arXiv:astro-ph/0512349
 Borgani, S. et al. 2004, MNRAS, 348, 1078, astro-ph/0310794
 Bulbul, G. E., Hasler, N., Bonamente, M., & Joy, M. 2010, ApJ, 720, 1038, 0911.2827
 Catalano, A. et al. 2014, ArXiv e-prints, 1402.0260
 Cavagnolo, K. W., Donahue, M., Voit, G. M., & Sun, M. 2009, ApJS, 182, 12, 0902.1802
 Cavaliere, A., & Fusco-Femiano, R. 1978, A&A, 70, 677
 Czakon, N. G. et al. 2015, ApJ, 806, 18, 1406.2800
 Dicker, S. R. et al. 2014, in Society of Photo-Optical Instrumentation Engineers (SPIE) Conference Series, Vol. 9153, Society of Photo-Optical Instrumentation Engineers (SPIE) Conference Series, 0
 Dicker, S. R. et al. 2008, in Society of Photo-Optical Instrumentation Engineers (SPIE) Conference Series, Vol. 7020, Society of Photo-Optical Instrumentation Engineers (SPIE) Conference Series, 0907.1306
 Ebeling, H., Edge, A. C., & Henry, J. P. 2001, ApJ, 553, 668
 Foreman-Mackey, D., Hogg, D. W., Lang, D., & Goodman, J. 2013, PASP, 125, 306, 1202.3665
 Glenn, J. et al. 1998, Proc. SPIE, 3357, 326
 Goodman, J., & Weare, J. 2010, Comm. App. Math. Comp. Sci., 5, 65
 Haig, D. J. et al. 2004, in Society of Photo-Optical Instrumentation Engineers (SPIE) Conference Series, Vol. 5498, Society of Photo-Optical Instrumentation Engineers (SPIE) Conference Series, ed. C. M. Bradford, P. A. R. Ade, J. E. Aguirre, J. J. Bock, M. Dragovan, L. Duband, L. Earle, J. Glenn, H. Matsuhara, B. J. Naylor, H. T. Nguyen, M. Yun, & J. Zmuidzinas, 78–94
 Hasselfield, M. et al. 2013, J. Cosmology Astropart. Phys., 7, 8, 1301.0816
 Hurier, G., Macías-Pérez, J. F., & Hildebrandt, S. 2013, A&A, 558, A118, 1007.1149
 Itoh, N., Kohyama, Y., & Nozawa, S. 1998, ApJ, 502, 7
 Jee, M. J. et al. 2009, ApJ, 704, 672, 0908.3897
 Jewell, P. R., & Prestage, R. M. 2004, in Society of Photo-Optical Instrumentation Engineers (SPIE) Conference Series, Vol. 5489, Ground-based Telescopes, ed. J. M. Oschmann, Jr., 312–323
 Joy, M. et al. 2001, ApJ, 551, L1
 Kitayama, T. et al. 2016, PASJ, 68, 88, 1607.08833
 Korngut, P. M. et al. 2011, ApJ, 734, 10, 1010.5494
 Kravtsov, A. V., & Borgani, S. 2012, ARA&A, 50, 353, 1205.5556
 Mantz, A., Allen, S. W., Rapetti, D., & Ebeling, H. 2010, MNRAS, 406, 1759, 0909.3098
 Mason, B. S. et al. 2010, ApJ, 716, 739, 0910.5025
 Maughan, B. J., Jones, C., Jones, L. R., & Van Speybroeck, L. 2007, ApJ, 659, 1125, astro-ph/0609690
 Maughan, B. J., Jones, L. R., Ebeling, H., & Scharf, C. 2004, MNRAS, 351, 1193, astro-ph/0403521
 Monfardini, A. et al. 2014, Journal of Low Temperature Physics, 176, 787, 1310.1230
 —. 2010, A&A, 521, A29, 1004.2209
 Mroczkowski, T. 2011, ApJ, 728, L35, 1101.2176
 Mroczkowski, T. et al. 2009, ApJ, 694, 1034, 0809.5077
 Muchovej, S. et al. 2007, ApJ, 663, 708, arXiv:astro-ph/0610115
 Nagai, D., Kravtsov, A. V., & Vikhlinin, A. 2007, ApJ, 668, 1, arXiv:astro-ph/0703661
 Planck Collaboration et al. 2014, A&A, 571, A29, 1303.5089
 —. 2013a, ArXiv e-prints, 1303.5081
 —. 2013b, A&A, 558, C2
 —. 2016, A&A, 594, A13, 1502.01589
 Reichardt, C. L. et al. 2013, ApJ, 763, 127, 1203.5775
 Romero, C. et al. 2016, ArXiv e-prints, 1608.03980
 Romero, C. E. et al. 2015, ApJ, 807, 121, 1501.00187
 Rumsey, C. et al. 2016, MNRAS, 460, 569, 1604.06120
 Ruppin, F. et al. 2017, A&A, 597, A110, 1607.07679
 Sarazin, C. L., Finoguenov, A., Wik, D. R., & Clarke, T. E. 2016, ArXiv e-prints, 1606.07433
 Sayers, J. et al. 2013, ApJ, 768, 177, 1211.1632
 Sayers, J., Golwala, S. R., Ameglio, S., & Pierpaoli, E. 2011, ApJ, 728, 39, 1010.1798
 Sayers, J. et al. 2016, ApJ, 832, 26, 1605.03541
 Vikhlinin, A., Markevitch, M., & Murray, S. S. 2001, ApJ, 549, L47, astro-ph/0008499